At-wavelength, system-level flare characterization of extreme-ultraviolet optical systems

Patrick Naulleau, Kenneth A. Goldberg, Eric M. Gullikson, and Jeffrey Bokor

The extreme-ultraviolet (EUV) phase-shifting point-diffraction interferometer (PS/PDI) has recently been developed to provide high-accuracy wave-front characterization critical to the development of EUV lithography systems. Here we describe an enhanced implementation of the PS/PDI that significantly extends its measurement bandwidth. The enhanced PS/PDI is capable of simultaneously characterizing both wave front and flare. PS/PDI-based flare characterization of two recently fabricated EUV 10×-reduction lithographic optical systems is presented. © 2000 Optical Society of America

OCIS codes: 090.0090, 110.1650, 110.2970, 120.2650, 120.3180, 120.3940, 120.5820, 260.7200.

1. Introduction

The quest to develop extreme-ultraviolet (EUV) optics for use in next-generation projection lithography systems providing sub-100-nm resolution has led to several recent innovations in EUV metrology.[1–3] One of these is the EUV phase-shifting point-diffraction interferometer (PS/PDI).[3–5] The EUV PS/PDI has been developed to provide the high-accuracy wave-front characterization critical to the development of EUV lithography systems. Operating at a wavelength near 13 nm, the reference wave-front accuracy of the PS/PDI has been demonstrated[6] to be better than $\lambda_{EUV}/350$ (0.04 nm) within a numerical aperture (NA) of 0.082, and the system has been successfully used to characterize and align several EUV optical systems.[7]

Thus far the PS/PDI has exclusively addressed the wave-front metrology issue. For lithographic-quality optics, however, it is equally important to consider flare. Caused by scatter from within the optical system, flare is the *halo* of light that surrounds the optical system point-spread function (PSF). The detrimental effects of flare include reduced contrast, which can lead to increased line-edge roughness in lithographic applications.

Flare characterization for EUV optics has typically relied on profilometry measurements performed on the individual optics and mathematical modeling to predict the effect the measured roughness has on flare. Previously, the only system-level at-wavelength flare test available involved printing. More recently, system-level EUV scatterometry-based[8] and PS/PDI-based[9] methods have been developed. Here we describe the latter in detail and present flare-measurement results from two recently fabricated EUV optical systems.

Because PS/PDI-based wave-front metrology measures the wave front at the exit pupil of the optical system, it is equivalent to PSF metrology (the wave front and the PSF form a Fourier-transform pair). For this reason flare can be characterized with wave-front metrology data, provided that it contains enough spatial-frequency bandwidth. In particular, the measured wave front should contain the mid-spatial-frequency range lying between the ranges commonly referred to as figure and finish. As previously implemented, the PS/PDI was incapable of accurately measuring the extended spatial-frequency band required for characterizing flare. Recent improvements made to the PS/PDI now allow the relevant spatial-frequency range to be measured.

The interferometric flare-measurement technique described here has advantages over flare-measurement techniques based on roughness characterization of individual optical components,[8] because it is a system-level measurement performed at the operational wavelength. Moreover, the interferometric method requires no additional data collec-

The authors are with the Center for X-Ray Optics, Lawrence Berkeley National Laboratory, Berkeley, California 94720. J. Bokor is also with the Department of Electrical Engineering and Computer Sciences, University of California, Berkeley, Berkeley, California 94720. P. Naulleau's e-mail address is pnaulleau@lbl.gov.

Received 8 November 1999.
0003-6935/00/172941-07$15.00/0

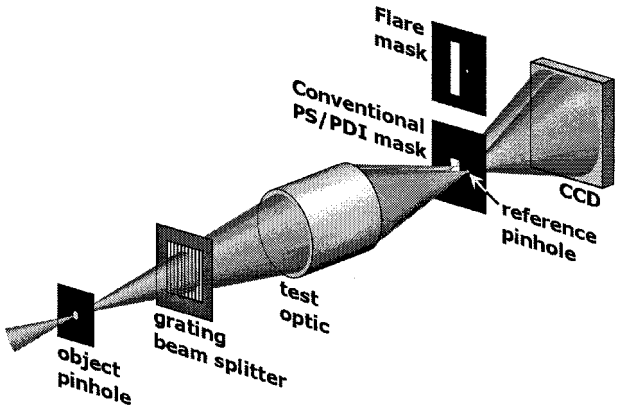

Fig. 1. Schematic of the PS/PDI. Both wave-front- and flare-measuring image-plane masks are shown.

tion beyond the data currently collected for EUV wave-front metrology. This aspect is important because the flare measurement imposes no additional test-time requirement and it eliminates the need for a separate test device. In practice, however, the PS/PDI-based system has a much lower spatial-frequency cutoff than do individual-component roughness characterization techniques. The PS/PDI-based system is, thus, best suited to measuring short-range flare (covering distances of less than approximately 500 times the diffraction-limited resolution). For a 0.1-μm-resolution EUV optical system, this distance is of the order of 50 μm. This technique also serves to validate conventional instrumentation methods applied to individual optical components and the mathematical models used to predict the system-level flare based on those measurements.[8]

Another significant benefit of the extended PS/PDI measurement bandwidth is that, in combination with EUV scattering measurements recently demonstrated[10] to have a dynamic range of ten orders of magnitude and measurement band ranging from 10^{-4} to 10^{-2} nm^{-1}, there now exist at-wavelength metrology capabilities covering the entire spatial-frequency range required for full characterization of EUV optics.

2. Description of the Phase-Shifting Point-Diffraction Interferometer

The PS/PDI is briefly described here; more complete descriptions have been previously published.[3,4] The PS/PDI is a variation of the conventional point-diffraction interferometer[11,12] in which a transmission grating has been added to greatly improve the optical throughput of the system and add phase-shifting capability. In the PS/PDI (Fig. 1) the optical system under test is coherently illuminated by a spherical wave generated by diffraction from a pinhole placed in the object plane. To ensure good quality of the spherical-wave illumination, the pinhole diameter is chosen to be several times smaller than the resolution limit of the optical system. A grating placed either before or after the test optic is used to split the illuminating beam, creating the required test and reference beams. A mask (the PS/PDI mask in Fig. 1) is placed in the image plane of the test optic to block the unwanted diffracted orders generated by the grating and to spatially filter the reference beam by use of a second pinhole (the reference pinhole), thereby removing the aberrations imparted by the optical system. The test beam, which also contains the aberrations imparted by the optical system, is largely undisturbed by the image-plane mask, because it passes through a window in the PS/PDI mask that is large relative to the diameter of the optical system PSF. The test and reference beams propagate to the mixing plane where they overlap to create an interference pattern that is recorded on a CCD detector.

3. Measuring Flare with the Phase-Shifting Point-Diffraction Interferometer

Because the image-plane mask is positioned in the Fourier plane of the measured wave front, it is apparent that the measurement spatial-frequency bandwidth is limited by the size of the image-plane test-beam window. This bandwidth translates directly to the image-plane distance over which the PS/PDI is capable of measuring flare.

The flare-measurement capabilities of the PS/PDI become more evident when we view the PS/PDI as a system that records an off-axis Fourier-transform hologram[13,14] of the optical system PSF. From this holographic point of view, the PSF, as observed through the test window, is the *object* distribution. Propagation from the image plane to the CCD in the far field performs the lensless Fourier-transform function. Furthermore, the reference pinhole provides the off-axis reference beam. Reconstruction of this electronic hologram yields a reconstructed image of the PSF including the tails (halo). The lateral extent of the reconstructed image is limited to the size of test window through which the PSF is observed. Thus the area over which the flare can be determined is simply the area of the test window. In the conventional EUV PS/PDI wave-front-measuring configuration, this area is typically a 3–5-μm-wide square.

To increase the flare-measurement range, the image-plane window size must be increased. Unambiguous holographic image reconstruction, however, limits the size of the window in the direction of the beam separation to ⅔ times the pinhole-to-window-center separation or smaller.[13,15] This ensures that the intermodulation term (zero order of the hologram) is fully separable from the carrier-modulated term (first order of the hologram) in the spatial-frequency domain. In the direction perpendicular to the pinhole separation, where the window can in principle be made arbitrarily long, the flare-measurement range is limited by the resolution of the detector and depends on the separation between the image plane and the detector.

Given a detector with pixel pitch T, the maximum measurable single-sided bandwidth is $1/(2T)$, half the spatial sampling rate of the detector, $f_s/2$. The

relationship between spatial frequencies recorded in the detector plane (f_x) and the spatial coordinates in the image plane (x) is $f_x \approx x/(\lambda z)$ with z being the distance between the two planes and λ the illumination wavelength. Thus the limit on measurable distance in the image plane is $|x| < \lambda z/(2T)$. For a detector-to-image-plane separation of 100 mm and a 24-μm pixel pitch (typical EUV PS/PDI parameters), this limit corresponds to a full-width measurement range of approximately 56 μm. Increasing the measurement bandwidth would require increasing the detector-to-image-plane separation or decreasing the detector pixel pitch; both are feasible.

Because the PS/PDI derives its reference beam by spatial filtering a laterally displaced copy of the test beam, a significant portion of the scattered light present in the image plane comes from the prefiltered reference beam. Simple holographic image reconstruction would erroneously combine the test beam with the scattered-reference light, yielding a deceptively high measure of the flare. This problem is further compounded by the fact that in practice the reference beam is made several times stronger than the test beam. This imbalance is used to compensate for pinhole-filtering losses and maintain adequate fringe visibility.[6] Fortunately, the reference-beam contamination problem can be overcome by use of the previously described PS/PDI dual-domain analysis method.[15]

The dual-domain technique was developed to eliminate scattered-reference-light contamination of PS/PDI wave-front data and is directly applicable to the flare-measurement problem of interest here. The method is essentially a three-tiered filtering system composed of low-pass spatial filtering the test-beam electric field, bandpass spatial filtering the individual interferogram irradiance frames of a phase-shifting series, and bandpass temporal filtering the phase-shifting series as a whole. The first step is physical and is performed by the test-beam window, whereas the final two steps are implemented numerically. The dual-domain method isolates the scattered-reference and test-beam light by recording a set of phase-shifted holograms and processing them in both the temporal and the spatial domains.

When the beam splitter is a binary-amplitude grating, as is typically the case for the EUV PS/PDI, a series of laterally displaced beams is formed in the image plane. These additional beams also contribute a small amount of scatter. Although the dual-domain method cannot fully eliminate the corruption from these higher-order diffraction terms, in practice the residual corruption is extremely small compared with the reference-beam corruption and can be compensated analytically.

When determining flare directly from the PSF, the dynamic range of the measurement is of great concern. The Fourier-transform holography method described here allows the PSF to be reconstructed with significantly larger dynamic range than could be achieved by direct imaging of the PSF onto the detector. This is because, with the Fourier-transform holography method, the recorded signal is relatively uniformly distributed across the detector, whereas in the direct imaging method the majority of the energy is concentrated in the small region near the PSF peak. In Section 4 the experimentally achieved dynamic range is demonstrated to be better than 10^7, whereas the inherent dynamic range of our 14-bit detector is only 16,384.

4. Experimental Results

The PS/PDI flare-measurement capability has been demonstrated with two EUV 10×-demagnification Schwarzschild objectives designed to operate at a wavelength of 13.4 nm.[16] The interferometry was performed with an undulator beamline[17] at the Advanced Light Source synchrotron radiation facility at Lawrence Berkeley National Laboratory. The beamline provides a tunable source of partially coherent EUV radiation with a coherence area significantly larger than the 0.75-μm object-plane pinhole used in the experiments described here.[18] The tests were performed at a wavelength of 13.4 nm with a bandwidth, $\lambda/\Delta\lambda$, of approximately 350. Here we report on the results obtained from two recently fabricated optics (subsequently referred to as B1 and B2). Both optics were developed to meet wave-front figure specifications of better than 0.8-nm rms[19,20] and flare specifications of less than 5% in an isolated, dark 4-μm line.

The flare mask, depicted in Fig. 2, was fabricated with electron-beam lithography and reactive-ion etching. The mask is made of a 200-nm-thick nickel absorbing layer evaporated on a 100-nm-thick silicon nitride (Si_3N_4) membrane. The features are etched completely through the membrane prior to the nickel evaporation. This leaves the pinholes and the windows as open-stencil features in the finished mask, thereby maximizing their transmission. The mask contains two orthogonal 3 μm × 30 μm windows, allowing anisotropic effects to be measured. Support bars were added to the windows, producing the paned structure seen in Fig. 2, to prevent the thin open-stencil membrane from rupturing. To mitigate the obscuring effect that these support bars have on the measurement, the reference pinhole is displaced from the window center in the direction parallel to the long axis of the window. This in turn allows the test beam to be displaced from the window center during the measurement. A properly chosen displacement eliminates all nulls in the radially averaged PSF data (also see Fig. 3). We further mitigate potential obscuration problems by providing two pinholes that allow separate measurements to be preformed where the PSF is displaced relative to the window by the pinhole separation, which is 2.5 μm. The small (0.3-μm-wide) protrusions in the center window portion were added as alignment aids.

The flare-measurement data-collection process involves acquiring a phase-shifting series of holograms (interferograms) of the optical system PSF. The phase shifting is accomplished by lateral translation of the grating beam splitter between exposures.

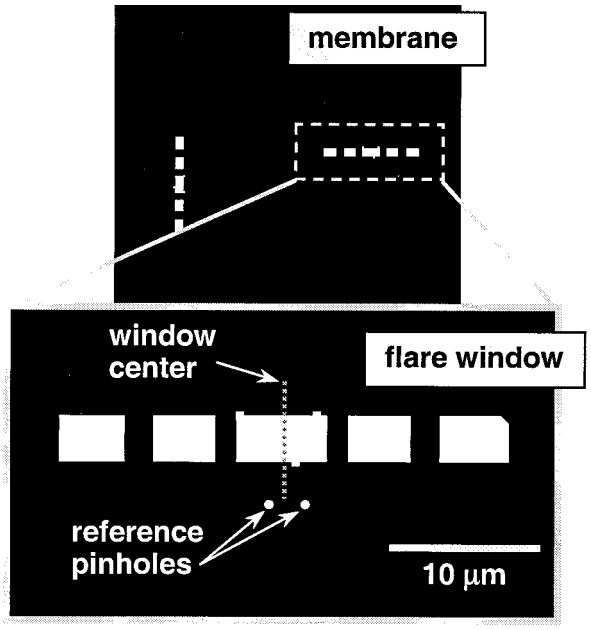

Fig. 2. Schematic of the 3 μm × 30 μm flare mask used for the measurement presented here. The mask contains two orthogonal windows, allowing anisotropic effects to be measured. Support bars were added to the windows to prevent the thin open-stenciled membrane from rupturing. To mitigate the obscuring effect that these support bars have on the measurement, the reference pinhole is displaced from the window center in the direction parallel to the long axis of the window. We further mitigate potential obscuration problems by providing two pinholes that allow separate measurements to be performed where the PSF is displaced relative to the window by the pinhole separation, which is 2.5 μm. The small (0.3-μm-wide) protrusions in the center window portion were added as alignment aids.

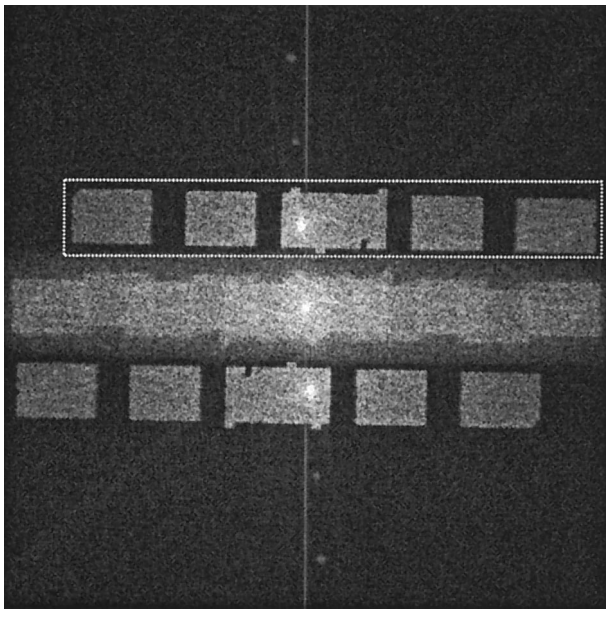

Fig. 3. Logarithmically scaled image of the Fourier transform of a representative hologram from the phase-shifting series. The Fourier-transform image represents the reconstructed image of the image-plane distribution. The dashed line highlights one of the holographic twin images.

Figure 3 shows a logarithmically scaled image of the Fourier transform of a representative hologram from the phase-shifting series acquired with optic B1. Because the recorded holograms are of the lensless Fourier-transform type, the Fourier transform displayed in Fig. 3 represents the reconstruction of the image-plane field distribution. The reconstructed image contains the customary twin images, and the intermodulation image.[13] The dashed line in Fig. 3 highlights one of the twin images, in which the image-plane window is clearly visible.

As with any physical imaging process, the resolution in the reconstructed image is determined by the NA of the measurement. This NA is limited by the smaller of (i) the extent of the reference beam or (ii) the physical extent of the detector. In practice we have typically found the detector size to be the limiting factor. In our case, where we have a detector size of 25.4 mm and a detector-to-image-plane distance of 100 mm, the measurement NA is 0.13, yielding a resolution of $1.22\lambda/\mathrm{NA} = 130$ nm. When the measurement NA is limited by the extent of the reference beam, the resolution can readily be shown to be equal to the pinhole size.

Having the reconstructed image of the image-plane distribution, we can determine the flare from the test-beam portion of the scatter seen in either one of the twin images. Because the simple Fourier-transform reconstruction of the PSF cannot distinguish between scatter in the test beam and scatter in the reference beam,[15] the halo observed in Fig. 3 is not an accurate representation of the flare. However, as described above, this problem can be overcome by use of the dual-domain data-acquisition and analysis method. During recording of phase-shifting data, the reference-beam scatter does not phase shift relative to the pinhole-diffracted reference light, because both components originate from the zero order of the grating. In contrast, the scattered test-beam light, which originates from the first-diffracted order of the grating, does phase shift relative to the pinhole-diffracted reference light. This distinction between the two scatter signals enables the reference-beam scatter component to be eliminated by use of the dual-domain processing technique.[15]

The apparent scatter outside the window region is a result of CCD and photon noise contributions. The mean value of this noise adds a dc bias to the measured scatter energy. This background noise is also present after dual-domain processing and, depending on its magnitude relative to the scattered-light magnitude, may need to be removed before determination of the flare. Because the noise is random in nature, it cannot be fully eliminated; however, its mean value can be removed by means of measuring and subtracting the average value of the apparent scatter in regions outside the image-plane window.

Figure 4 shows a logarithmically scaled image of the dual-domain-reconstructed intensity PSF for optic B1. We obtained these data by first applying the

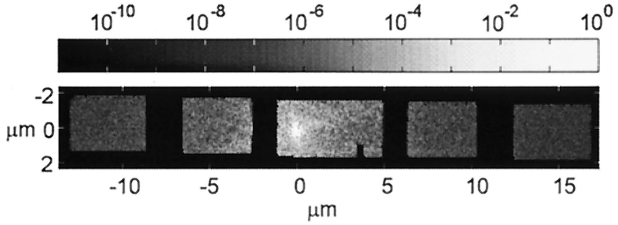

Fig. 4. Logarithmically scaled image of the dual-domain-reconstructed intensity PSF from optic B1. The PSF shown is an average of three independent measurements. Invalid-data regions due to image-plane window obscuration are masked.

dual-domain analysis method to the acquired phase-shifting series to recover the complex-amplitude field in the plane of the detector and then by Fourier transforming the field. The PSF shown is an average of three independent measurements. The data dropouts are caused by the aforementioned bars in the test window. As described above, however, the off-window-center PSF peak ensures that scattering data are available at all radial distances from the PSF peak.

Once we have calculated the corrected PSF, it is possible to characterize the flare. To this end we find the normalized scatter-energy density as a function of radial distance from the PSF peak, $S(r)$. This is simply the radially averaged PSF,

$$S(r) = \frac{1}{2\pi r}\int \mathrm{PSF}(r, \theta)\mathrm{d}\theta. \tag{1}$$

Performing this calculation on the PSF in Fig. 4 yields an energy density with a radial decay that is well approximated by r^n, where $n = -3.10 \pm 0.01$. The quoted uncertainty was determined from the standard deviation of the three independent measurements.

Because the test window is elongated in one direction only, the scatter-energy-density results may be biased if the scatter is anisotropic. To assess the significance of this potential problem, the measurement is repeated with a window oriented in the orthogonal direction. The orthogonal direction is found to have a scatter-energy radial decay well approximated by r^n, where $n = -3.03 \pm 0.05$. The small difference between the two directions indicates slight anisotropic scattering effects.

Combining the results from the two orthogonal directions leads to the scatter energy depicted in Fig. 5. The imperfect Airy lobes are caused by aberrations in the optic. Figure 5 demonstrates an effective dynamic range of better than 10^7. To predict the flare expected in a typical imaging situation, the scatter-energy density must be known over the full radial extent of the field. For the optics considered here, the full field size is 250-μm radius in the image plane. The extended-range scatter-energy density can be obtained by extrapolation of the interferometrically determined data or by use of data derived from profilometry performed on the individual substrates before assembly of the optical system. To avoid possible extrapolation errors, we chose the latter. The plot in Fig. 5 shows an overlay of the scatter-energy density predicted from profilometry. The two measurement methods have overlapping data in the radial range from 1 to 16 μm, and good agreement between the two methods is evident.

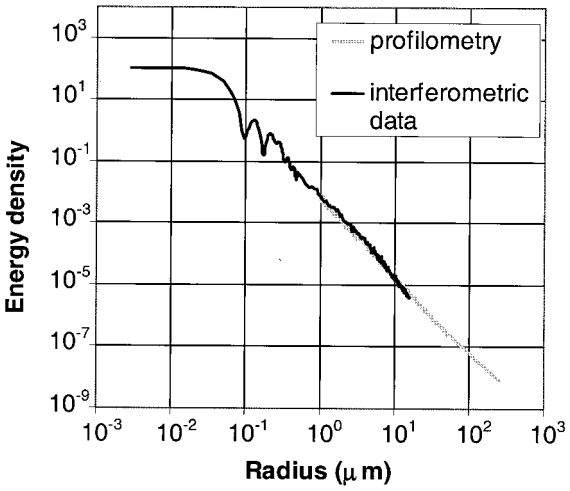

Fig. 5. Comparison of the scatter-energy density as a function of radial separation from the PSF peak determined by the PS/PDI- and the profilometry-based methods, respectively (optic B1).

From the full-field scatter it is now possible to predict the flare, defined here as

$$\mathrm{flare} = \frac{E_t - E_s}{E_t}, \tag{2}$$

where E_t is the total PSF energy in the field of interest and E_s is the specular energy in the field. We defined the specular energy as the PSF energy contained within the feature size of interest. Figure 6

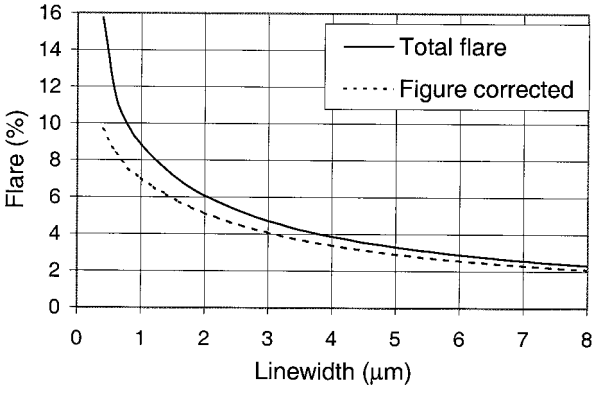

Fig. 6. Calculated flare in an isolated line as a function of linewidth with a 250-μm-radius image-field size. Also shown is the figure-corrected flare derived by removal of the flare that would be calculated, given a smooth yet aberrated optic. For the high-quality optics under consideration here this is essentially the flare one would calculate from an ideal Airy pattern. The figure-corrected flare calls out the flare caused by roughness alone (optic B1).

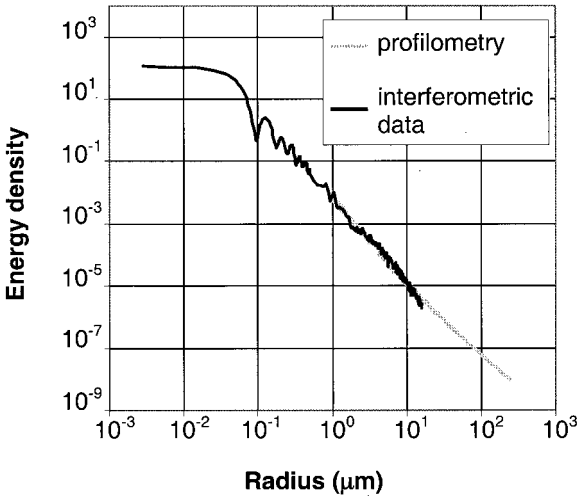

Fig. 7. Comparison of the scatter-energy density as a function of radial separation from the PSF peak determined by the PS/PDI- and the profilometry-based methods, respectively (optic B2).

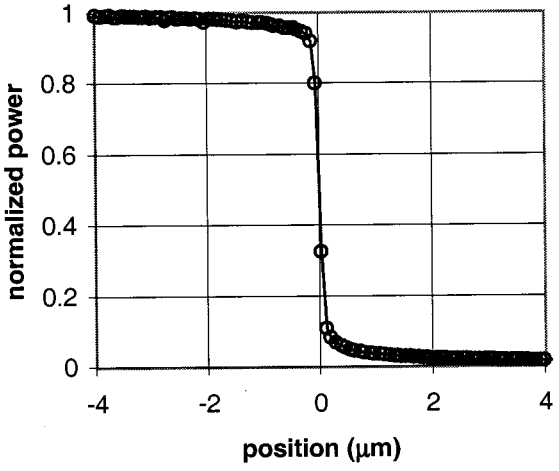

Fig. 9. Shown are 8-μm EUV scatterometry edge scan results for optic B1. The data have been normalized to the centered position detector current. The flare in a 4-μm line determined by this method is 4.5%.

shows a plot of the flare in an isolated line as a function of linewidth for a 250-μm-radius field of view. The flare in a 4-μm line is (3.9 ± 0.1)%, better than the 5% fabrication target for this optic. The flare value predicted by profilometry alone is 4.0%.[8] Also shown in Fig. 6 is the *figure-corrected* flare derived by removal of the flare that would be calculated given a smooth yet aberrated optic (figure error only). For the high-quality optics under consideration here, this figure-corrected flare is essentially the flare one would calculate from the tails of an ideal Airy pattern. Although the figure-corrected flare is not representative of the contrast one might expect in the aerial image, it does isolate the flare caused by roughness alone: The roughness-induced flare in a 4-μm line is 3.4%.

Repeating the same measurements and analysis on optic B2 yields the PSF and flare results shown in Figs. 7 and 8. As expected, the results are very similar to those obtained from optic B1. For optic B2 the total flare in a 4-μm line is (3.2 ± 0.1)%, whereas that predicted by profilometry alone is 3.0%.[8]

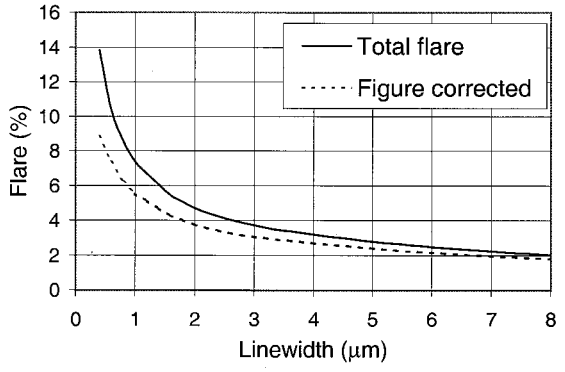

Fig. 8. Calculated flare in an isolated line as a function of linewidth with a 250-μm-radius image-field size. Also shown is the figure-corrected flare (optic B2).

The flare measurements presented here were also verified with an EUV scatterometry technique.[8] The scatterometry method works by placement of a photodiode behind a field-sized aperture in the image plane. A subresolution pinhole in the object plane illuminates the optic coherently. With the diode and the aperture centered on the image point, the total energy in the field of interest, E_t, is measured. The specular component of the beam is then found by translation of the aperture and the diode and by use of the aperture edge to perform a knife-edge test. This test is conveniently performed with the PS/PDI experimental setup by means of replacing the image-plane mask with the aperture–diode combination. Figure 9 shows results from a 8-μm edge scan for optic B1. The data have been normalized to the current corresponding to the total energy in the field of interest, E_t. The flare in a 4-μm line determined by this method is 4.5%.

5. Conclusion

The measurement bandwidth of the PS/PDI has been significantly extended. This new capability, in turn, allows the PS/PDI to be used as an at-wavelength flare-characterization tool. The improved PS/PDI provides a system-level flare test that can be performed in parallel with wave-front metrology. The system has been successfully used to characterize two recently fabricated low-flare 10×-reduction EUV lithographic optics, and the results are in close agreement with other flare-measurement techniques.

The authors are greatly indebted to Erik Anderson for nanofabrication of masks, to Phil Batson for engineering support, and to the entire Center for X-Ray Optics (CXRO) staff for enabling this research. Special thanks are due to Paul Denham for expert assistance with experimental control systems. This research was supported by the Extreme Ultraviolet Limited Liability Company, the Semiconductor Re-

search Corporation, the Defense Advanced Research Projects Agency (DARPA) Advanced Lithography Program, and the U.S. Department of Energy (DOE) Office of Basic Energy Science.

References

1. J. E. Bjorkholm, A. A. MacDowell, O. R. Wood II, Z. Tan, B. LaFontaine, and D. M. Tennant, "Phase-measuring interferometry using extreme ultraviolet radiation," J. Vac. Sci. Technol. B **13,** 2919–2922 (1995).
2. A. K. Ray-Chaudhuri, W. Ng, F. Cerrina, Z. Tan, J. Bjorkholm, D. Tennant, and S. J. Spector, "Alignment of a multilayer-coated imaging system using extreme ultraviolet Foucault and Ronchi interferometric testing," J. Vac. Sci. Technol. B **13,** 3089–3093 (1995).
3. H. Medecki, E. Tejnil, K. A. Goldberg, and J. Bokor, "Phase-shifting point diffraction interferometer," Opt. Lett. **21,** 1526–1528 (1996).
4. K. A. Goldberg, "Extreme ultraviolet interferometry," Ph.D. dissertation (University of California, Berkeley, Calif. 1997).
5. E. Tejnil, K. A. Goldberg, S. H. Lee, H. Medecki, P. J. Batson, P. E. Denham, A. A. MacDowell, J. Bokor, and D. Attwood, "At-wavelength interferometry for EUV lithography," J. Vac. Sci. Technol. B **15,** 2455–2461 (1997).
6. P. Naulleau, K. A. Goldberg, S. Lee, C. Chang, D. Attwood, and J. Bokor, "Extreme-ultraviolet phase-shifting point-diffraction interferometer: a wave-front metrology tool with subangstrom reference-wave accuracy," Appl. Opt. **38,** 7252–7263 (1999).
7. K. A. Goldberg, P. Naulleau, and J. Bokor, "EUV interferometric measurements of diffraction-limited optics," J. Vac. Sci. Technol. B **17,** 2982–2986 (1999).
8. E. Gullikson, S. Baker, J. Bjorkholm, J. Bokor, K. Goldberg, J. Goldsmith, C. Montcalm, P. Naulleau, E. Spiller, D. Stearns, J. Taylor, and J. Underwood, "EUV scattering and flare from 10× projection cameras," in *Emerging Lithographic Technologies III*, Y. Vladimirski, ed., Proc. SPIE **3676,** 717–723 (1999).
9. P. Naulleau, K. A. Goldberg, E. Gullikson, and J. Bokor, "Interferometric at-wavelength flare characterization of EUV optical systems," J. Vac. Sci. Technol. B **17,** 2987–2991 (1999).
10. E. M. Gullikson, "Scattering from normal incidence EUV optics," in *Emerging Lithographic Technologies II*, Y. Vladimirski, ed., Proc. SPIE **3331,** 72–80 (1998).
11. W. Linnik, "A simple interferometer to test optical systems," Proc. Acad. Sci. USSR **1,** 210–212 (1933).
12. R. N. Smartt and W. H. Steel, "Theory and application of point-diffraction interferometers," Jpn. J. Appl. Phys. **14,** Suppl. 14-1, 351–356 (1975).
13. E. N. Leith and J. Upatnieks, "Reconstructed wavefronts and communication theory," J. Opt. Soc. Am. **52,** 1123–1130 (1962).
14. E. N. Leith and J. Upatnieks, "Wavefronts reconstruction with diffused illumination and three-dimensional objects," J. Opt. Soc. Am. **54,** 1295–1302 (1964).
15. P. Naulleau and K. A. Goldberg, "Dual-domain point diffraction interferometer," Appl. Opt. **38,** 3523–3533 (1999).
16. D. A. Tichenor, G. D. Kubiak, M. E. Malinowski, R. H. Stulen, S. J. Haney, K. W. Berger, R. P. Nissen, R. L. Schmitt, G. A. Wilkerson, L. A. Brown, P. A. Spence, P. S. Jin, W. C. Sweat, W. W. Chow, J. E. Bjorkholm, R. R. Freeman, M. D. Himel, A. A. MacDowell, D. M. Tennant, O. R. Wood II, W. K. Waskiewicz, D. L. White, D. L. Windt, and T. E. Jewell, "Development and characterization of a 10× Schwarzschild system for SXPL," in *Soft X-Ray Projection Lithography*, A. M. Hawryluk and R. H. Stulen, eds., Vol. 18 of OSA Proceedings Series (Optical Society of America, Washington, D.C., 1993), pp. 79–82.
17. R. Beguiristain, J. Underwood, M. Koike, P. Batson, E. Gullikson, K. Jackson, H. Medecki, and D. Attwood, "High flux undulator beam line optics for EUV interferometry and photoemission microscopy," in *High Heat Flux Engineering III*, A. M. Khounsary, ed., Proc. SPIE **2855,** 159–169 (1996).
18. D. Attwood, P. Naulleau, K. Goldberg, E. Tejnil, C. Chang, R. Beguiristain, P. Batson, J. Bokor, E. Gullikson, M. Koike, H. Medecki, and J. Underwood, "Tunable coherent radiation in the soft x-ray and extreme ultraviolet spectral regions," IEEE J. Quantum Electron. **35,** 709–720 (1999).
19. K. A. Goldberg, P. Naulleau, R. Gaughan, H. Chapman, J. Goldsmith, and J. Bokor, "Direct comparison of EUV and visible-light interferometries," in *Emerging Lithographic Technologies III*, Y. Vladimirski, ed., Proc. SPIE **3676,** 635–642 (1999).
20. J. Goldsmith, K. Berger, D. Bozman, G. Cardinale, D. Folk, C. Henderson, D. O'Connell, A. Ray-Chaudhuri, K. Stewart, D. Tichenor, H. Chapman, R. Gaughan, R. Hudyma, C. Montcalm, E. Spiller, J. Taylor, J. Williams, K. Goldberg, E. Gullikson, P. Naulleau, and J. Cobb, "Sub-100-nm imaging with the EUV 10× microstepper," in *Emerging Lithographic Technologies III*, Y. Vladimirski, ed., Proc. SPIE **3676,** 264–271 (1999).